ASSESSMENT OF NUMERICAL APPROACHES FOR QUASI-STATIC, FATIGUE, AND DYNAMIC PROPAGATION OF DELAMINATION IN CURVED LAMINATES

Maikel Khella[1], Pietro Ballarin[1], Carlos G. Dávila[2], Alessandro Airoldi[1]

[1]Dept. of Aerospace Science and Technology, Politecnico di Milano, Via La Masa, 34, 20156 Milano, Italy

[2]Durability, Damage Tolerance, and Reliability Branch, NASA Langley Research Center, Hampton, VA 23601, USA

Keywords: Composites; Carbon fibre; Delamination; Fatigue; Numerical analysis

ABSTRACT

The accurate prediction of fatigue delamination growth and critical damage size remains an open challenge in enabling the Slow-Growth design and damage-tolerance substantiation in composite aircraft structures. Delamination is especially important due to difficult detectability and the high sensitivity of laminated composites to this failure mode. This work presents a preliminary experimental characterization of the fatigue-driven delamination in a thick, pre-damaged L-shaped composite specimen. To support and interpret these results, a cohesive zone-based finite element (FE) fatigue modelling framework was first verified on standard Mode I (DCB), Mode II (ENF), and Mixed-Mode (MMB) specimens, using experimental data from the literature. The framework was then applied to simulate the fatigue behaviour of the L-shaped specimen. Finally, the variation of energy release rate with crack-growth was investigated to explain the observed failure modes, highlighting the strong sensitivity of delamination growth to initial loading conditions.

1 INTRODUCTION

Laminated composite structures are inherently susceptible to out-of-plane loading, with delamination initiating at stress levels significantly lower than those required for in-plane failure. Low-velocity impacts frequently induce internal delaminations that may not be externally visible but compromise structural performance. Delamination disrupts interlaminar stress transfer, inhibiting load redistribution mechanisms between plies and reduces sustainable load in compression. The FAA Advisory Circular AC 20-107A [1] addresses damage tolerance in composite structures, particularly for Category 2 barely visible impact damages, which may reduce residual strength below the Ultimate Load (UL) but never below Limit Load (LL). Three substantiation approaches are identified: (i) no-growth, where damage is stable over inspection intervals; (ii) arrested-growth, where propagation halts before reaching a critical size; and (iii) slow-growth, allowing controlled propagation, which is monitored via scheduled inspections. Slow-growth design leads to greater structural efficiency than no-growth but requires predictive models for both residual strength and fatigue crack growth [2]. Consequently, finite element (FE) models used for a slow-growth design of composite structures must reliably predict (i) residual static strength in the presence of damage, and (ii) delamination growth under cyclic loading.

Existing models for static delamination strength are well-established while, in contrast, fatigue modelling remains an active research area. Traditional FE-based fatigue models [3], [4], [5], [6], [7], [8], typically rely on Paris-law parameters and fracture mechanics inputs, which pose significant experimental and computational demands. Recently, a simplified S-N-based framework for the FE simulation of fatigue loading of structures has been proposed [9], [10], [11], using a two-step Simple Cyclic Loading (SCL) method based on a monotonic preload followed by a constant-amplitude fatigue step that activates the fatigue damage accumulation. Different versions of such functions have been proposed. The most recent version of fatigue damage accumulation function, presented in [10], is empirical in nature, and it is calibrated via Paris rate data and two fitting parameters for each delamination mode, I and II. While initial calibrations in the literature are manual (trial and error), an automated procedure is also possible [12].

The studies presented in the literature are typically focused on the development and validation of fatigue damage accumulation functions at the coupon levels, considering different propagation modes and levels of severity. This work investigates the crack growth in thick L-shaped laminates containing a pre-existing delamination (at a critical interface) under fatigue loading. Specimens were tested under a tensile opening configuration, which induces an interlaminar tensile stress state in the curved zone of the specimens that promotes crack growth. Despite the large amount of research work on the inelastic quasi-static response of L-shaped and curved structural elements, studies on their fatigue behavior are rare. An accurate analysis and comparison between quasi-static and fatigue failure modes is presented in [14,15] for unidirectional and cross-ply L-shaped laminates without pre-damage. In the present research activity, attention is focused on the analysis of crack growth regimes and rate. Moreover, the predictive capabilities of a modelling approach based on fatigue damage accumulation laws are presented, outlining the potential and the challenges for the application of these methods to the prediction of growth rates in structural elements.

2 EXPERIMENTS ON L-SHAPED COMPOSITE LAMINATES

Fatigue tests were conducted on pre-delaminated, L-shaped, thick-laminate specimens with a width of 20 mm, promoting an interlaminar mode I crack propagation by applying loads at the ends of the arms. The geometry, shown in Figure 1-(a), is representative of curved laminates that are typically prone to delamination in aeronautical composite structures. In particular, the experimental activity aims to support broader efforts in characterizing slow-growth fatigue behaviour in thick curved composite elements of rotorcraft structures. In Figure 1-(b), the experimental setup is presented. Loads were applied through hinged grips clamping the first 30 mm of each leg. Fatigue tests were conducted in displacement control with a displacement ratio $R = 0.1$ and a frequency of 5 Hz. Maximum and minimum forces and the cycle count were recorded throughout the test.

All specimens were manufactured from AS4/8552 unidirectional (UD) prepreg, with the layup $[0]_{48}$ using the manufacturer-recommended cure cycle. The nominal cured ply thickness is 0.13 mm [13], resulting in a total nominal laminate thickness of 6.24 mm. The material elastic properties and the most significant interlaminar properties for the presented activity are reported in Table 1, where G_{Ic} is the critical energy release rate for mode I, and σ_{c0} is the interlaminar tensile strength.

E_{11T} [MPa]	E_{11C} [MPa]	$E_{22}=E_{33}$ [MPa]	$G_{12}=G_{13}$ [MPa]	G_{23} [MPa]	$\nu_{12}=\nu_{13}$ [-]	ν_{23} [-]	G_{Ic} [kJ/m^2]	σ_{c0} [MPa]	G_{IIc} [kJ/m^2]	τ_{c0} [MPa]
127,277	111,488	9239	4826	3553	0.302	0.3	0.26	105	0.87	128

Table 1: AS4/8552 elastic and interlaminar properties [13] and [14]

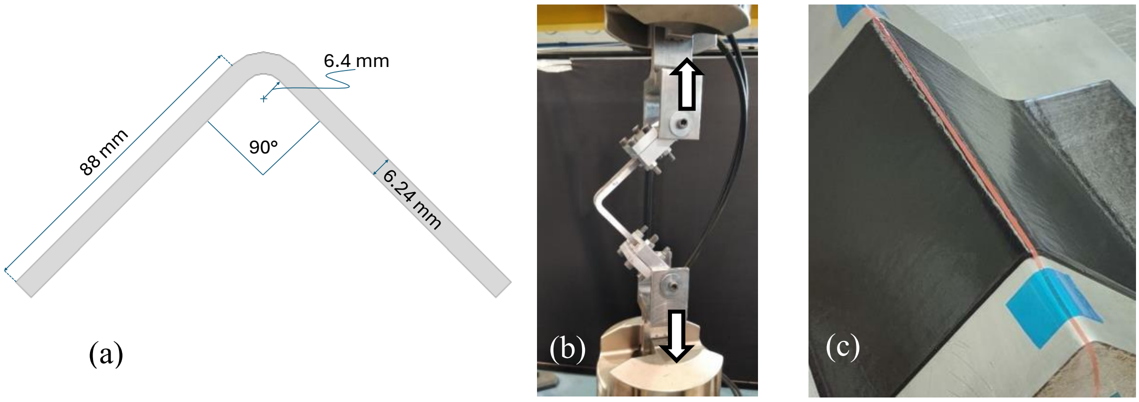

Figure 1: Specimen dimensions (a), test set-up (b), and pre-delamination placement (c)

All the specimens were manufactured with a 2-mm long artificial delamination induced with a Teflon film placed at the centre of the curved region, at one-third through the thickness (between the 16th and 17th plies). This location corresponds to the region of maximum interlaminar tensile stress for the considered load condition [15]. (Figure 1-(c)).

Before fatigue testing, two static tests were conducted to evaluate the way in which damage progresses (Figure 2). In both tests, the initial linear-elastic phase in which the defect did not propagate was followed by a sudden load drop (Figure 2-(a)). The drop corresponds to an unstable growth from the pre-delamination through the whole curved region (Figure 2-(c)). Further loading extended the crack into the specimen legs (Figure 2-(d)), which is reflected in the reduction of the secant stiffness in the force–displacement curves.

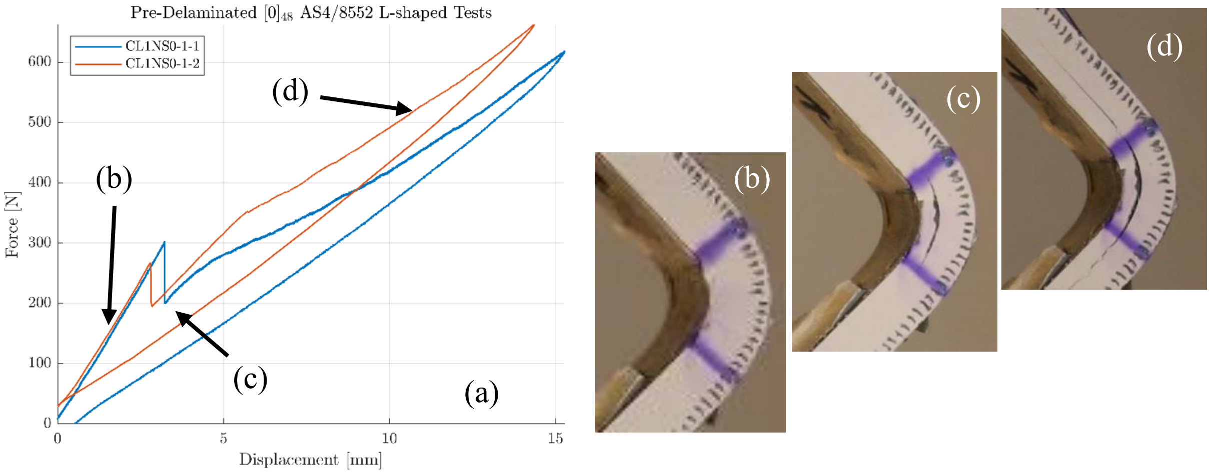

Figure 2: Static tests on L-shaped specimens

Fatigue tests were performed on five specimens in displacement control. Initial test severities were derived from the static tests (Figure 2), as a function of the displacement at the onset of unstable delamination propagation. Assuming an initial linear elastic response, fatigue loading levels were selected to correspond to a target load severity (defined in terms of strain energy release rate), scaled from the critical propagation value δ_{crit} (at delamination onset under static loading), using the relation:

$$\frac{G_{max}}{G_{crit}} = Severity = \frac{\delta_{max}^2}{\delta_{crit}^2} \tag{1}$$

where δ_{max} is the maximum applied displacement in fatigue. The Irwin-Kies equation, $G = \frac{P^2}{2B}\frac{dC}{da}$, was used, where P is the applied load, C the specimen compliance, B the specimen width, and a the crack length. Table 2 summarizes the nominal load-levels decided for the fatigue test, the corresponding maximum displacements, and the corresponding G-severities (all with a displacement ratio R=0.1). Two specimens were tested at high severity levels (0.90 and 0.75) and three specimens were tested with a nominal severity of about 0.60. The effective displacement and force levels were adjusted considering the response of each specimen and the discrepancies with the nominal levels are also due the presence of mechanical plays and contact tolerances in the test setup. Regarding the codes used to identify specimens, the first number indicates the specific production batch they were cut from, and the second is a number specific to each.

Specimen name	CL1NF0-1-4	CL1NF0-1-5	CL1NF0-2-3	CL1NF0-2-1	CL1NF0-2-4
F_{max} (nominal)	270 N	220 N	160 N	160 N	160 N
δ_{max}	2.688 mm	2.272 mm	1.870 mm	1.670 mm	1.700 mm
G-severity	0.90	0.75	0.62	0.55	0.57
F_{max} (effective)	269 N	222 N	165 N	159 N	160 N

Table 2: Specimens tested under fatigue loading, the initial test severity and the test maximum displacement (R = 0.1)

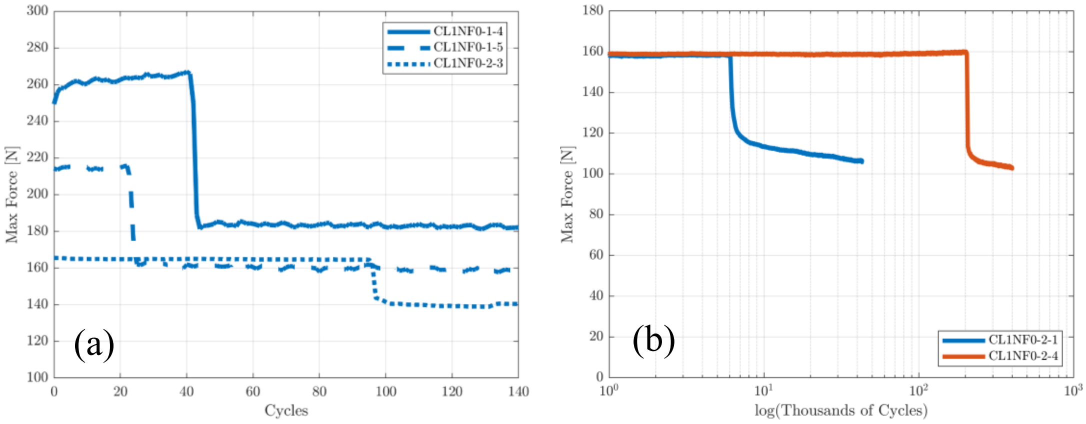

Figure 3: Max force during L-shaped fatigue tests: (a) Highest severity tests, (b) CL1NF0-2-1 and CL1NF0-2-4

The two specimens CL1NF0-1-4 and CL1NF0-1-5, tested at the highest severity, underwent a rapid delamination propagation within very few cycles (41 and 22 load cycles, respectively). The rapid drop of the force shown in Figure 3-(a) is a consequence of the rapid crack growth, which accelerated abruptly from the Teflon insert (initial defect length of 2 mm) along the curved region. Crack growth rate was significantly reduced after a specific load, which was 189 N for specimen CL1NF0-1-4 and 162 N for CL1NF0-1-5. The load drop was obtained in 3 cycles for CL1NF0-1-4, as well as for CL1NF0-1-5 (about 0.5 s)

The three specimens tested at the lowest severities (in the range 0.55 to 0.62) provided different responses. The trend of force vs. cycles for the specimen CL1NF-2-3 (effective severity 0.62) is plotted with those of the highest severities tests in Figure 3-(a), since it exhibited a similar rapid crack propagation just after 95 load cycles, with a force drop from 164 N to 141 N, in 6 cycles (about 1 s). Considering the test at 0.55 severity level (blue curve in CL1NF0-2-1, Figure 3-(b)), the number of cycles required to reach the region of rapid force drop increased to approximately 6000 cycles, and the rapid force drop went on until about 140 N after 40 cycles (about 6.5 s). The subsequent test was conducted at the same nominal load level (red curve in CL1NF0-2-4, Figure 3-(b)). It obtained the same qualitative response, with an initial stable force level followed by a rapid growth of the crack, but the onset of the rapid crack propagation required about 204,000 cycles. The rapid force drop arrested at about 139 N after 83 cycles (about 14 s).

During fatigue testing, damage accumulates at the pre-existing delamination tip until a critical threshold is reached, triggering a rapid crack propagation across the curved region, which corresponds to the load drop that was observed in the different tests. The load drop is not instantaneous, as in the unstable propagations that occurred in quasi-static tests, and its velocity tends to decrease if severity is reduced. Prior to this event, load fluctuations were minimal, indicating negligible crack growth. The initial rapid growth is arrested at different load levels. Thereafter, the load decreases gradually as the delamination extends into the specimen legs. This behaviour highlights the existence of a threshold for the onset of the accelerated crack propagation phase and a transition from such phase to a slow crack propagation activated after a certain propagation length. The number of cycles required for these transitions vary from a few cycles to tens or hundreds of thousands of cycles, with maximum values that were obtained only in the tests with the lower severity levels.

In the quasi-static tests, the initial crack undergoes an initial unstable propagation. The propagation regime then changes to a stable slow-growth regime when the crack, approximately, reaches the end of the curved zones. Assuming a constant crack resistance for the material, such response is indicative of a strong variation of the Energy Release Rate (ERR) available to promote crack propagation with the crack length. In the fatigue tests, despite the quantitative differences in the number of cycles required to activate fast crack propagation, the qualitive responses are very similar for all the five tests. Although the propagations observed in the fatigue testing were not instantaneous, the occurrence of two regimes in the fatigue crack growth is evident in all the fatigue tests performed. The interpretation of these phenomena requires an analysis of the ERR variation, which is accomplished in the next section by applying the Irwin-Kies equation, linking the compliance of the specimens to the crack propagation. The simulations of these type of propagation with the fatigue damage accumulation laws validated for characterization specimens, like DCB and ENF, is particularly challenging due to the expected gradients in ERR and the presence of unstable propagation regimes in the quasi-static tests. The large scatter exhibited by the specimens tested at a nominal severity around 0.60 should be investigated, although such variability in fatigue test results is consistent with literature on similar specimens [16], [17], which emphasizes the need to model the statistical distributions of interfacial properties in fatigue analyses more than static ones.

3 NUMERICAL COMPLIANCE AND ENERGY RELEASE RATE EVOLUTION WITH CRACK LENGTH

The evaluation of the ERR for different crack lengths was performed via semi-analytical assessment based on the Irwin-Kies equation:

$$G = \frac{F^2}{2B}\frac{dC}{da} \tag{3}$$

This relation links applied load F, the specimen compliance C (or, better said, the effect of specimen geometry characteristics as a function of crack-length a) to the strain energy release rate G, the energy available for crack growth. A finite element model of the specimen was developed in Abaqus Standard [18] to numerically evaluate the compliance as a function of crack length.

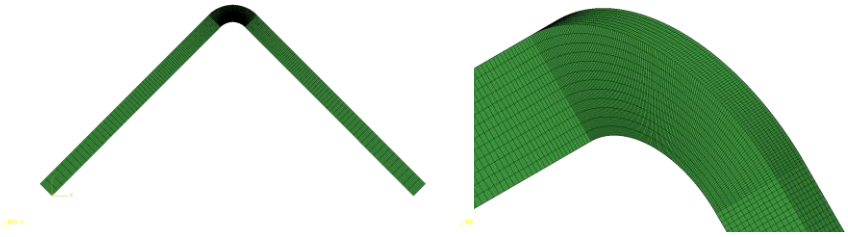

Figure 4: FE model of the angular specimen

The model is a 2-mm-wide strip of the specimen, meshed with laminated continuum shell elements (SC8R). Each shell comprises 4 plies A layer of zero-thickness cohesive elements (*COH3D8*) – containing a pre-crack at the centre of the curved region – was inserted between the 16th and 17th plies (i.e., between the 4th and 5th continuum shell layers). A total of 8 elements was used across the width. The mesh is coarse at the extremities of the legs and becomes finer in the curved region, where elements are approximately 0.1 mm long. Material properties are those reported Table 1. Loading was simulated by applying opening displacements to rigid bodies including the last 30 mm of each leg. Such boundary conditions were applied to the reference nodes of the rigid bodies, positioned in correspondence of the hinges. Free rotations were allowed around the grip hinge axis, which replicates experimental boundary conditions. An implicit static analysis procedure was used, allowing for non-linear geometrical effects. Damage in cohesive elements was inhibited since the objective of these analyses was simply to evaluate the compliance at different crack lengths. A series of analyses was performed by removing cohesive elements in 0.2 mm increments to represent the development of an ideal crack from 1 mm to 13.4 mm (i.e., until the end of the curved region). The crack was symmetrically extended at both crack-tips. The compliances obtained in each analysis were interpolated with a polynomial, proving the result reported in Figure 5-(a) and then derived. By applying Eq. 3, the variation of the ERR with the crack length *a* was evaluated, as reported in Figure 5-(b), considering the load corresponding to an opening of 2 mm.

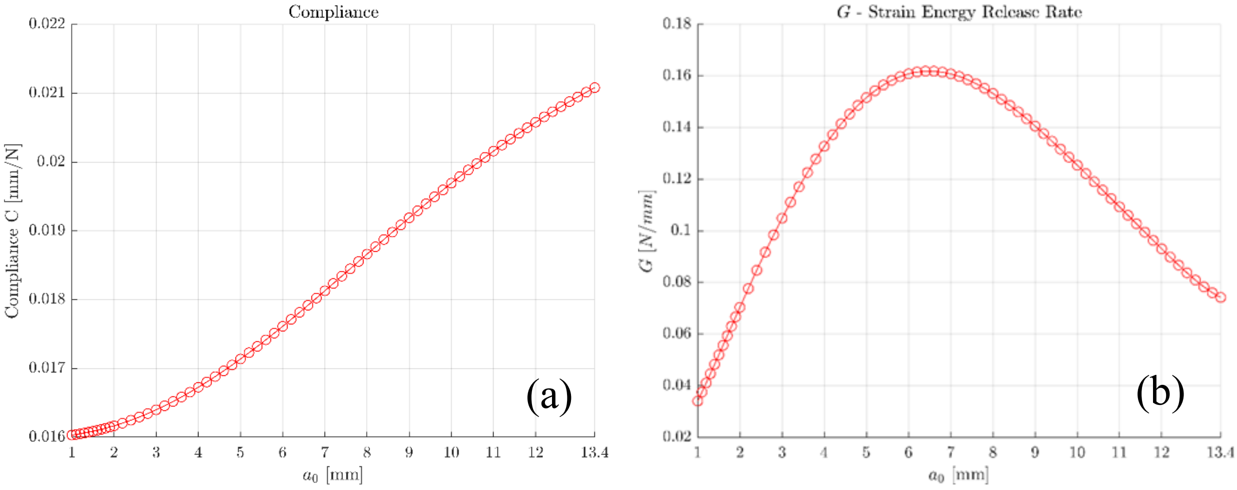

Figure 5: Numerical Compliance (a) and Energy Release Rate (b) of the L-shaped specimen as a function of crack length

Assuming a constant crack resistance, the sign of the derivative of the ERR curve, dG/da, determines the crack propagation regime: unstable if $dG/da > 0$ and stable if $dG/da < 0$. According to Figure 5-(b), the existence of a transition between unstable and stable regimes is evidenced at *a* = 6.4 mm. These results are consistent with those reported in [19], [20], where a similar approach was used to calculate G and the stability of delamination propagation in L-shaped laminates. Despite the differences in specimen geometry and loading conditions, the existence of a threshold for unstable-to-stable crack growth transition was found beyond a certain crack length (*a* = 6.55 mm in [18]).

This approach does not consider the presence of any fracture process zone (FPZ) at the crack tip. An estimate for the length can be evaluated using the formulation in [21]:

$$l_{pz}^{ss} = \gamma \frac{E' G_c}{\sigma_c^2} \text{ where } E' = \frac{E_{22}}{Q}, \; Q = \frac{1}{2}\sqrt{2\left[\sqrt{\frac{E_{22}}{E_{11}}} - \nu_{21}\right] + \frac{E_{22}}{G_{12}}} \qquad (4)$$

which, using the values for γ reported in [22] ($\gamma = 0.73$) and [23] ($\gamma = 1.00$) and the material properties in Table 1, yields 0.16 mm and 0.22 mm as upper and lower bounds for the FPZ length. Although the process zone can be considered small, these values could affect the evaluation of the compliance as a function of the crack length used to obtain the results in Figure 5.

The experimental results can be interpreted by using the results of the semi-analytical procedure presented above. Since the tests were performed at fixed opening, the evolution of force and the relation between the compliance and the crack length in Figure 5-(a) can be used to estimate the crack length during the fatigue tests. The results, for the specimens tested with the lowest severity levels are similar. For CL1NF0-2-3, where rapid propagation was triggered after 95 cycles, the rapid crack growth was arrested at a force level that is compatible with a crack length of 7.5 mm. For the specimens CL1NF0-

2-1 and CL1NF0-2-4, the estimated crack lengths at the end of the rapid crack growth is of 6.7 mm and 7.2 mm. All these values are slightly beyond the maximum in the ERR-a curve, indicating the phase of rapid propagation ends when the crack enters the region of stable crack growth. For the specimens tested at the highest severity levels (CL1NF0-1-4 and CL1NF0-1-5), the estimation provides values larger than 13 mm. Such results can be explained by considering that the elastic energy stored in the specimens promoted a propagation of the crack into the region of stable propagation.

4 NUMERICAL SIMULATIONS

4.1 Static failure modelling

The same finite element model developed for the evaluation of the compliance with crack growth, was used to perform quasi-static simulation through a fully non-linear analysis, adopting an explicit time integration scheme with Simulia Abaqus/Explicit. The explicit solver can capture unstable propagation phenomena and transition to stable regimes without the convergence difficulties that are common with implicit codes. The model retains the continuum shell (SC8R) representation of the specimen, including the zero-thickness cohesive interface elements (COH3D8) positioned between the 16th and 17th interfaces, where the defect was located. The model was subjected to an opening displacement at the reference points coupled to the specimen legs. Quasi-static conditions were ensured by imposing a smoothly varying opening time history, and by checking that reaction forces read at the two reference points were identical. A user-defined Cohesive Zone Model (CZM) was used to characterize the fracture process. The CZM in [24], originally conceptualized for static fracture, was implemented in a VUMAT subroutine for COH3D8/COH2D4 cohesive elements in Abaqus/Explicit. The model is characterized by an initial linear elastic response (of penalty stiffness K_p). Damage initiates at the cohesive strength σ_0 (at the displacement δ_0) and progresses, gradually reducing the stress carrying capability according to a linear softening law, until a displacement δ_f, where the work spent in the damage process equals the prescribed interface toughness. The critical ERR and strengths used in the analyses are reported in Table 1 [14]. A quadratic strength criterion for damage initiation and the B-K model for damage progression were selected for mixed-mode propagation. The penalty stiffness was set at 1.25E+05 N/mm^3, following the formulation in [25].

The simulated force-displacement response in the analysis of the L-shaped specimen is presented in Figure 6, together with the corresponding experimental curves of the two specimens tested. The model accurately captures the linear elastic stiffness of the specimen during initial loading, as well as the predicted load at the onset of unstable delamination propagation from the pre-crack, which matches closely with the experimental failure loads.

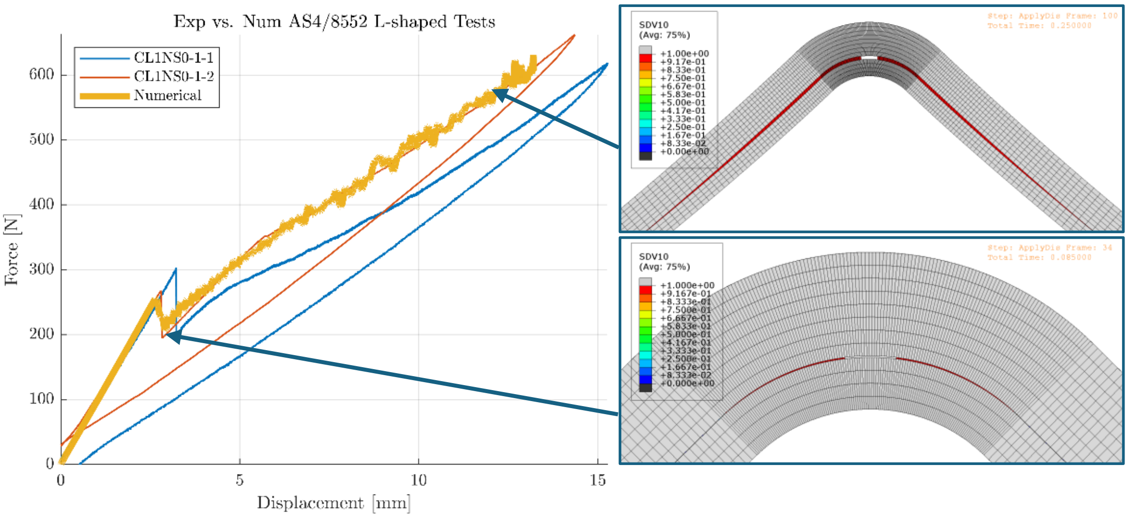

Figure 6: Numerical vs Experimental tests on L-shaped specimen

The sudden load drop that accompanies unstable delamination growth through the curved region was also captured by the simulation, as well as the response during the stable propagation of the crack along the legs of the specimens. This successful correlation of the static force-displacement response (including stiffness, first failure load, load drop, and crack stable propagation) provides confidence in the capability of the modelling approach to reliably model the loads required to propagate the initial delamination in quasi-static simulations, both for stable and unstable propagation regimes.

4.2 Modelling of fatigue damage accumulation and crack growth

Examples of cycle-by-cycle FE fatigue simulations exist in the literature but are only practical for Low and Ultra-Low Cycle Fatigue (LCF, ULCF) situations, which involve very few cycles with large plastic strains (such as seismic loading of steel structures [26]). For High Cycle Fatigue (HCF) applications, involving millions of cycles, simulating every cycle is computationally prohibitive. Therefore, simplified strategies are necessary for the practical FE simulation of structures under fatigue. A common class of simulation approaches is that of the "envelope load" methods [27]. They consist in the modelling of only the maximum (and/or minimum) loads in a fatigue load block, while relying on the CZM constitutive law to capture damage accumulation due to fatigue. Among the possible methods, the Simplified Cyclic Loading (SCL) is the one adopted here: it involves the quasi-static loading up to the block maximum load, after which fatigue damage accumulation is activated and continued, either until a specified cycle count or the (static) structural failure. A fatigue damage accumulation law can be easily integrated in the VUMAT subroutine previously used for quasi-static simulations. The fatigue model used here is based on Dávila's approach [9], [10], [11], using the SCL method and the suggested damage accumulation function, calibrated by fitting two parameters to the Paris data for mode I and II. The model applied is an updated version of the original approach proposed in [9] (CF18). It is based on the evaluation of a damage norm D. At each step in the simulation, the new values of the quasi-static and fatigue damage variables are evaluated independently of each other, and the larger of the two is selected as the one to be passed on to the next time increment. The typical response of a bi-linear cohesive zone element is shown in Figure 7-(a), showing the fatigue damage progression on a single cohesive element under a constant maximum stress. Load is applied quasi-statically from $\sigma = 0$ to $\sigma = \sigma_{max}$, and then kept constant while fatigue damage accumulates. As fatigue damage is accumulated, the damage norm degrades the penalty stiffness and λ increases. The traction-displacement state at the material point evolves along the path denoted as "Fatigue" in Figure 7-(a), until the softening branch of the static cohesive law is reached, at a displacement jump λ^*, at which point, the cohesive response is dominated by static tearing, which goes on until full separation of the cohesive interface.

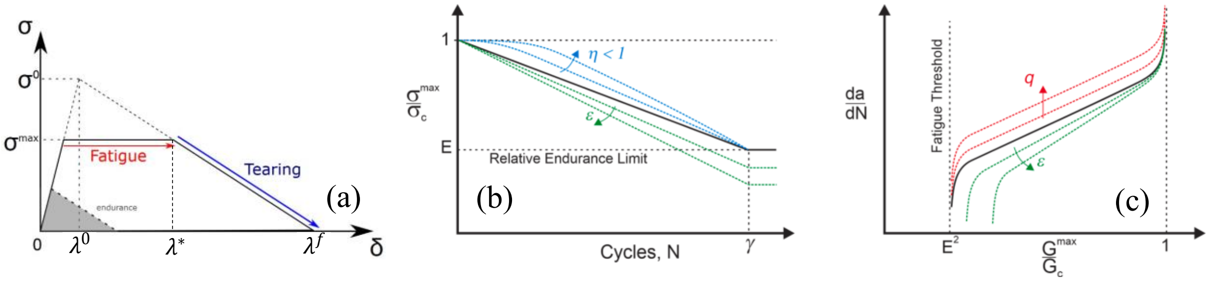

Figure 7: Fatigue damage accumulation law: (a) single element response in fatigue simulation, (b) effects of parameters η and ε in the S-N curve, and (c) effect of parameters q and ε in the Paris Curve

The CF22 fatigue damage accumulation law proposed in [11] is used herein within a VUMAT for explicit simulations. CF22 expresses the rate of change of the damage norm, D, with load cycles, N:

$$\frac{dD}{dN} = \frac{(1-D)^{-q}}{\gamma\, E^{\beta}(\beta+q+1)} \left(\frac{\lambda}{\lambda^*}\right)^{\beta} \tag{5}$$

where λ/λ^* is the ratio of current cohesive displacement jump λ to the corresponding static fracture displacement λ^* at the current residual fracture toughness; q is a fitting parameter to be calibrated, while

β, E and γ are parameters with a precise physical meaning in the S-N curve of the material. E is the infinite-life endurance threshold normalized with the static strength, i.e., the maximum allowable stress amplitude below which fatigue life is infinite, and γ is the number of cycles corresponding to this endurance limit. The threshold E is differentiated for the two opening modes, depends on the stress-ratio, and is interpolated between Mode I and Mode II endurance thresholds:

$$E = E_I + B(E_{II} - E_I) \text{ where: } E_I = \frac{2\varepsilon}{\varepsilon+1+R(\varepsilon-1)}\,,\ E_{II} = min\left(0.999,\ \phi\left(\left(\frac{2}{1-R}\right)^{\varpi}\right)\right) \tag{6}$$

here, ε and ϕ are the relative endurance values at fully reversed loading ($R = -1$) for Mode I and II, respectively; ϖ is a parameter controlling the variation of E_{II} as a function of R, and B is the mode mixity. The parameters β and q in Equation 5 are expressed as follows:

$$\beta = \frac{\eta \log(\gamma)}{\log(E)}\,,\ q = q_I + B(q_{II} - q_I) \tag{7}$$

where η is the brittleness parameter, and q_I and q_{II} parameters that allow the fitting of Paris crack growth rates in Mode I and II. The effect of the model parameters in the S-N curve and in the growth rate vs. severity plots are represented in Figure 7-(b) and Figure 7-(c), respectively. The calibration of the fatigue damage accumulation law for the AS4/8552 unidirectional (UD) prepreg was obtained via a trial-and-error procedure in [11]. Since the material is the same as used for the L-shaped specimens described in Section 2, the same calibration was adopted for the simulation of the fatigue tests.

In the explicit time integration scheme, each time step corresponds to a number of cycles ΔN. By discretizing the expression in Equation 5, the current value of the fatigue damage norm can be evaluated, as in Equation 8.

$$\frac{\Delta D}{\Delta N} = \frac{(1-D_{k-1})^{-q}}{\gamma\, E^{\beta}(\beta+q+1)}\left(\frac{\lambda}{\lambda^*}\right)^{\beta} \rightarrow D_k = D_{k-1} + \frac{(1-D_{k-1})^{-q}}{\gamma\, E^{\beta}(\beta+q+1)}\left(\frac{\lambda_k}{\lambda^*{}_k}\right)^{\beta} \Delta N \tag{8}$$

The fictitious frequency that links simulation time with cycle is selected to keep ΔD small enough at each integration step to avoid the numerical instabilities associated with excessive damage increments, but large enough to avoid a waste of computational power.

4.3 Simulation of the L-shaped specimen under fatigue loading

This section presents the results of simulations of the fatigue tests on the L-shaped laminated specimen. Figure 8 shows fatigue simulation results for specimens CL1NF0-1-5, tested at an initial severity of 0.70, and CL1NF0-2-1, at an initial severity of 0.55. Specimen CL1NF0-1-4 reaches the onset of unstable propagation during the quasi-static loading phase, so its fatigue simulation was not possible.

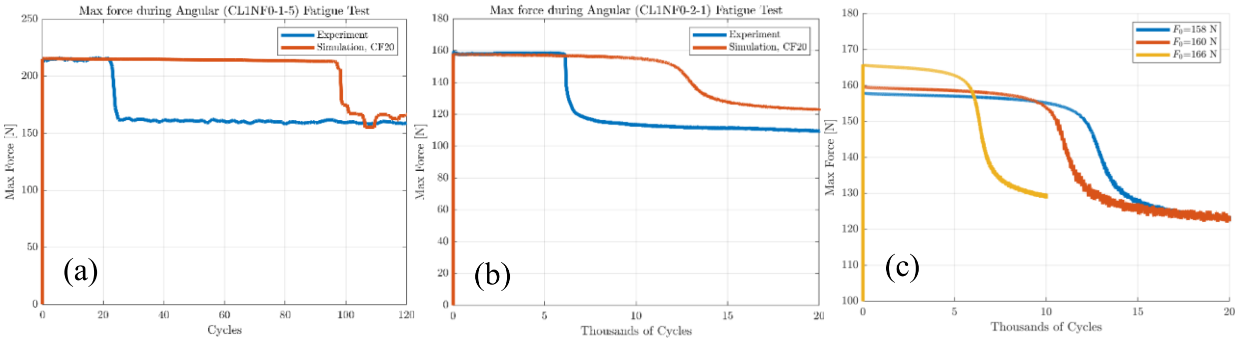

Figure 8: FE simulations compared with experimental fatigue tests on L-shaped specimens

The FE analyses show the onset of a rapid crack propagation after few cycles in CL1NF0-1-5 (96 cycles against 22 cycles in the test) and the need of thousands of cycles to activate the same phenomenon in CL1NF0-2-1, where the model predicts the threshold at approximately 12,000 cycles, about twice the observed 6100 cycles. Considering the scatter of the experimental tests, the results are promising. In the CL1NF0-1-5 simulation, the crack growth is almost instantaneous and is arrested at a force level that matches the experimental level. In the simulation of CL1NF0-2-1, conducted at a severity of 0.55, the rate of the force reduction, related to the crack growth rate, is lower in the simulation than in the test. Moreover, the total crack propagation in the fast phase of the growth is lower than the experimental one, as indicated by the higher force level.

Despite these discrepancies, the qualitative aspects of the response are captured in both cases. Considering noticeable experimental variation of the response for the three tests performed at severity levels of 0.55, 0.57, and 0.62, two additional simulations were performed by applying slightly different openings, corresponding to 158 N and 166 N. The results are compared in Figure 8-(c) with the simulation performed at 160 N, already presented in Figure 8-(b). As can be seen, small variations in the applied load produce a large variation in the number of cycles required to activate the rapid growth propagation from 6000 to 12,500 cycles.

5 CONCLUSIONS

In this work, a study of delamination propagation under quasi-static and cyclic loading in L-shaped specimens was presented. Different regimes of propagation were found in quasi-static tests, in agreement with the results obtained with a semi-analytical evaluation of the ERR, through the application of an Irwin-Kies analysis. In the fatigue tests, very different quantitative responses were obtained by varying different severity levels, although three phases could be identified in all the experiments: a first phase of nucleation, without crack growth, a second phase of rapid crack growth, at a rate increasing with the severity, and a third phase of slow growth of the crack.

The availability of the ERR vs. crack length curve obtained through the semi-analytical procedure made possible an interpretation of the results. The energy available for crack opening increases with a significant gradient from the pre-cracked conditions until a crack length of about 6.4 mm (from 0.06 kJ/m2 to 0.16 kJ/m2 for an opening of 2 mm). This means the severity imposed at the beginning of the tests increases rapidly as the crack grows, promoting a very fast propagation phase. Interestingly, the experimental results indicate that this phase of rapid crack propagation ends after the maximum of the ERR curve, when severity starts decreasing with crack length.

The application of a cohesive-based approach within FE explicit simulation was able to capture the response in quasi-static tests. A fatigue damage accumulation law available in literature was described, implemented in a user-defined material subroutine and applied to model the fatigue tests. The three phases of the fatigue responses were qualitatively reproduced, with quantitative discrepancies that can be difficult to interpret, considering the limited number of experiments and the relevancy of typical scattering in fatigue propagation of delamination documented in the literature. The application of explicit time integration schemes made possible the identification of different propagation regimes with a good level of reliability. Results are promising for the possible application of the proposed approach in the presence of large variation of ERR with crack advancement, which can induce significantly different crack propagation rates in real-world damage scenarios.

REFERENCES

[1] "AC 20-107A - Composite Aircraft Structure." Accessed: May 22, 2025. [Online]. Available: https://www.faa.gov/regulations_policies/advisory_circulars/index.cfm/go/document.information/documentID/22052

[2] J. A. Pascoe, "Slow-growth damage tolerance for fatigue after impact in FRP composites: Why current research won't get us there," *Theoretical and Applied Fracture Mechanics*, vol. 116, p. 103127, Dec. 2021, doi: 10.1016/J.TAFMEC.2021.103127.

[3] B. L. V. Bak, A. Turon, E. Lindgaard, and E. Lund, “A simulation method for high-cycle fatigue-driven delamination using a cohesive zone model,” *Int J Numer Methods Eng*, vol. 106, no. 3, pp. 163–191, Apr. 2016, doi: 10.1002/NME.5117.

[4] B. L. V. Bak, A. Turon, E. Lindgaard, and E. Lund, “A benchmark study of simulation methods for high-cycle fatigue-driven delamination based on cohesive zone models,” *Compos Struct*, vol. 164, pp. 198–206, Mar. 2017, doi: 10.1016/J.COMPSTRUCT.2016.11.081.

[5] L. Carreras *et al.*, “A simulation method for fatigue-driven delamination in layered structures involving non-negligible fracture process zones and arbitrarily shaped crack fronts,” *Compos Part A Appl Sci Manuf*, vol. 122, pp. 107–119, Jul. 2019, doi: 10.1016/J.COMPOSITESA.2019.04.026.

[6] L. Carreras, B. L. V. Bak, S. M. Jensen, C. Lequesne, H. Xiong, and E. Lindgaard, “Benchmark test for mode I fatigue-driven delamination in GFRP composite laminates: Experimental results and simulation with the inter-laminar damage model implemented in SAMCEF,” *Compos B Eng*, vol. 253, p. 110529, Mar. 2023, doi: 10.1016/J.COMPOSITESB.2023.110529.

[7] G. G. Trabal, B. L. V. Bak, B. Chen, L. Carreras, and E. Lindgaard, “An adaptive floating node based formulation for the analysis of multiple delaminations under high cycle fatigue loading,” *Compos Part A Appl Sci Manuf*, vol. 160, p. 107036, Sep. 2022, doi: 10.1016/J.COMPOSITESA.2022.107036.

[8] A. Turon, J. Costa, P. P. Camanho, and C. G. Dávila, “Simulation of delamination in composites under high-cycle fatigue,” *Compos Part A Appl Sci Manuf*, vol. 38, no. 11, pp. 2270–2282, Nov. 2007, doi: 10.1016/J.COMPOSITESA.2006.11.009.

[9] C. G. Dávila, “From S-N to the Paris law with a new mixed-mode cohesive fatigue model for delamination in composites,” *Theoretical and Applied Fracture Mechanics*, vol. 106, p. 102499, Apr. 2020, doi: 10.1016/J.TAFMEC.2020.102499.

[10] C. G. Dávila and M. W. Joosten, “A cohesive fatigue model for composite delamination based on a new material characterization procedure for the Paris law,” *Eng Fract Mech*, vol. 284, p. 109232, May 2023, doi: 10.1016/J.ENGFRACMECH.2023.109232.

[11] C. G. Davila, C. A. Rose, G. B. Murri, W. C. Jackson, and W. M. Johnston, “Evaluation of Fatigue Damage Accumulation Functions for Delamination Initiation and Propagation,” 2020. Accessed: May 23, 2025. [Online]. Available: http://www.sti.nasa.gov

[12] I. Leciñana, J. Zurbitu, J. Renart, and A. Turon, “A robust fatigue parameter determination method for a local fatigue cohesive zone model,” *Int J Fatigue*, vol. 171, p. 107582, Jun. 2023, doi: 10.1016/J.IJFATIGUE.2023.107582.

[13] Y. Ng, J. Tomblin, and E. Hooper, “Hexcel 8552 AS4 Unidirectional Prepreg at 190 gsm & 35% RC Qualification Material Property Data Report FAA Special Project Number SP4614WI-Q,” 2011.

[14] S. Ghiasvand, “Modeling and monitoring of interface damage in composite in the presence of residual and combined stress states,” 2023, Accessed: Jul. 01, 2025. [Online]. Available: https://www.politesi.polimi.it/handle/10589/183798

[15] W. C. Jackson and R. H. Martin, “An Interlaminar Tensile Strength Specimen,” *ASTM Special Technical Publication*, no. 1206, pp. 333–354, 1993, doi: 10.1520/STP12638S.

[16] B. Tasdemir and D. Coker, “Comparison of damage mechanisms in curved composite laminates under static and fatigue loading,” *Compos Struct*, vol. 213, pp. 190–203, Apr. 2019, doi: 10.1016/J.COMPSTRUCT.2019.01.072.

[17] B. Tasdemir and D. Coker, “Fatigue and static damage in curved woven fabric carbon fiber reinforced polymer laminates,” *J Compos Mater*, vol. 56, no. 11, pp. 1693–1708, Jun. 2022, doi: 10.1177/00219983221078787/ASSET/82CB5E67-A985-4ADF-B041-3E44CFE1EB10/ASSETS/IMAGES/LARGE/10.1177_00219983221078787-FIG19.JPG.

[18] “Abaqus 2016 Documentation.” Accessed: Jun. 29, 2025. [Online]. Available: http://130.149.89.49:2080/v2016/index.html

[19] R. H. Martin, “Delamination Failure in a Unidirectional Curved Composite Laminate,” *ASTM Special Technical Publication*, no. 1120, pp. 365–383, 1992, doi: 10.1520/STP20170S.

[20] G. Wimmer and H. E. Pettermann, “A semi-analytical model for the simulation of delamination in laminated composites,” *Compos Sci Technol*, vol. 68, no. 12, pp. 2332–2339, Sep. 2008, doi: 10.1016/J.COMPSCITECH.2007.10.022.

[21] A. Airoldi and C. G. Dávila, “Identification of material parameters for modelling delamination in the presence of fibre bridging,” *Compos Struct*, vol. 94, no. 11, pp. 3240–3249, Nov. 2012, doi: 10.1016/J.COMPSTRUCT.2012.05.014.

[22] G. Bao and Z. Suo, “Remarks on Crack-Bridging Concepts,” *Appl Mech Rev*, vol. 45, no. 8, pp. 355–366, Aug. 1992, doi: 10.1115/1.3119764.

[23] A. Hillerborg, M. Modéer, and P. E. Petersson, “Analysis of crack formation and crack growth in concrete by means of fracture mechanics and finite elements,” *Cem Concr Res*, vol. 6, no. 6, pp. 773–781, Nov. 1976, doi: 10.1016/0008-8846(76)90007-7.

[24] P. P. Camanho and C. G. Dávila, “Mixed-Mode Decohesion Finite Elements for the Simulation of Delamination in Composite Materials,” NASA/TM-2002-211737, 2002.

[25] A. Turon, C. G. Dávila, P. P. Camanho, and J. Costa, “An engineering solution for mesh size effects in the simulation of delamination using cohesive zone models,” *Eng Fract Mech*, vol. 74, no. 10, pp. 1665–1682, Jul. 2007, doi: 10.1016/J.ENGFRACMECH.2006.08.025.

[26] H. R. Amiri, A. A. Aghakouchak, S. Shahbeyk, and M. D. Engelhardt, “Finite element simulation of ultra low cycle fatigue cracking in steel structures,” *J Constr Steel Res*, vol. 89, pp. 175–184, Oct. 2013, doi: 10.1016/J.JCSR.2013.07.007.

[27] B. L. V. Bak, C. Sarrado, A. Turon, and J. Costa, “Delamination under fatigue loads in composite laminates: A review on the observed phenomenology and computational methods,” *Appl Mech Rev*, vol. 66, no. 6, Nov. 2014, doi: 10.1115/1.4027647/443639.

[28] T. K. O’Brien, A. D. Chawan, R. Krueger, and I. L. Paris, “Transverse tension fatigue life characterization through flexure testing of composite materials,” *Int J Fatigue*, vol. 24, no. 2–4, pp. 127–145, Feb. 2002, doi: 10.1016/S0142-1123(01)00104-9.